

PAPER • OPEN ACCESS

Blue- and red-shifts of V_2O_5 phonons in NH_3 environment by *in situ* Raman spectroscopy

To cite this article: Amos Adeleke Akande *et al* 2018 *J. Phys. D: Appl. Phys.* **51** 015106

View the [article online](#) for updates and enhancements.

You may also like

- [Understanding anion-redox reactions in cathode materials of lithium-ion batteries through *in situ* characterization techniques: a review](#)

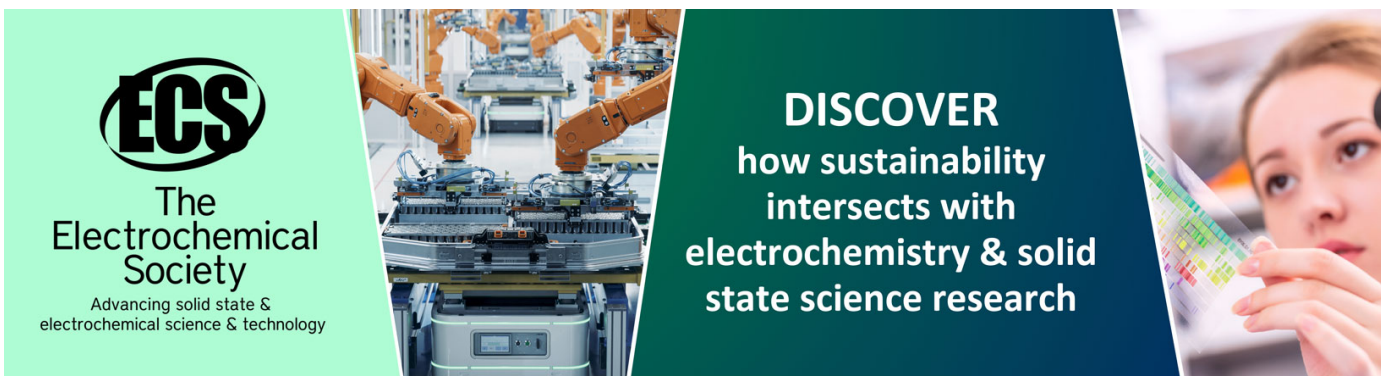
Ye Yeong Hwang, Ji Hyun Han, Sol Hui Park *et al.*

- [In situ Raman spectroscopy of \$LiFePO_4\$: size and morphology dependence during charge and self-discharge](#)

Jing Wu, Gopi Krishna Phani Dathar, Chunwen Sun *et al.*

- [Quantifying the interfacial load transfer in electrospun carbon nanotube polymer nanocomposite microfibers by using *in situ* Raman micromechanical characterization techniques](#)

Ohood Q Alsmairat, Feilin Gou, Christopher M Dmuchowski *et al.*



ECS
The
Electrochemical
Society
Advancing solid state &
electrochemical science & technology

DISCOVER
how sustainability
intersects with
electrochemistry & solid
state science research

Blue- and red-shifts of V₂O₅ phonons in NH₃ environment by *in situ* Raman spectroscopy

Amos Adeleke Akande^{1,2} , Augusto Goncalo Jose Machatine²,
Bathusile Masina³, George Chimowa¹, Boitumelo Matsoso⁴, Kittessa Roro⁵,
Mart-Mari Duvenhage⁶, Hendrik Swart⁶, Jayita Bandyopadhyay¹,
Suprakas Sinha Ray¹ and Bonex Wakikunga¹

¹ DST/CSIR National Centre for Nano-Structured Materials, PO Box 395, Pretoria 0001, South Africa

² Department of Physics, University of Pretoria, Pretoria, 0002, South Africa

³ CSIR-National Laser Centre, PO Box 395, Pretoria, 0001, South Africa

⁴ School of Chemistry, DST-NRF Centre of Excellence in Strong Materials and the Molecular Sciences Institute, University of the Witwatersrand, Johannesburg, Wits 2050, South Africa

⁵ Energy Centre, Council for Scientific and Industrial Research, PO Box 395, Pretoria 0001, South Africa

⁶ Physics Department, University of the Free State, Free State, South Africa

E-mail: aaakande@csir.co.za (Amos A Akande) and bmwakikunga@csir.co.za (Bonex Mwakikunga)

Received 18 August 2017, revised 26 October 2017

Accepted for publication 8 November 2017

Published 5 December 2017



CrossMark

Abstract

A layer of ~30 nm V₂O₅/100 nm-SiO₂ on Si was employed in the *in situ* Raman spectroscopy in the presence of NH₃ effluent from a thermal decomposition of ammonium acetate salt with the salt heated at 100 °C. When the layer is placed at 25 °C, we observe a reversible red-shift of 194 cm⁻¹ V₂O₅ phonon by 2 cm⁻¹ upon NH₃ gas injection to saturation, as well as a reversible blue-shift of the 996 cm⁻¹ by 4 cm⁻¹ upon NH₃ injection. However when the sensing layer is placed at 100 °C, the 194 cm⁻¹ remains un-shifted while the 996 cm⁻¹ phonon is red-shifted. There is a decrease/increase in intensity of the 145 cm⁻¹ phonon at 25 °C/100 °C when NH₃ interacts with V₂O₅ surface. Using the traditional and quantitative gas sensor tester system, we find that the V₂O₅ sensor at 25 °C responds faster than at 100 °C up to 20 ppm of NH₃ beyond which it responds faster at 100 °C than at 25 °C. Overall rankings of the NH₃ gas sensing features between the two techniques showed that the *in situ* Raman spectroscopy is faster in response compared with the traditional chemi-resistive tester. Hooke's law, phonon confinement in ~51 nm globular particles with ~20 nm pore size and physisorption/chemisorption principles have been employed in the explanation of the data presented.

Keywords: V₂O₅, VO₂, *in situ* Raman sensing, blue-shift, red-shift, selectivity, phonons

 Supplementary material for this article is available [online](#)

(Some figures may appear in colour only in the online journal)

1. Introduction

Semiconductor metal oxide gas chemo-resistive sensors have been a preferred transduction or method of detecting flammable, combustible, poisonous and toxic gases for many years



Original content from this work may be used under the terms of the [Creative Commons Attribution 3.0 licence](#). Any further distribution of this work must maintain attribution to the author(s) and the title of the work, journal citation and DOI.

now. Since its inception in 1960, when scientists discovered changes in the conductivity of semiconductor materials in the presence of gas and air [1–3], chemo-resistive technique has been a major means of transducing chemical and physical signals by converting them into a measurable one. Among other modern gas sensors or transducers such as electrochemical [4], optical [5], acoustic [6]; the metal oxide chemi-resistor is more applicable in real-life practical devices due to the characteristics such as low cost, long lifetime, fast response

time and high sensitivity [3]. However, the ability to selectively adsorb or detect a certain species or type of gas/analyte has been the limiting factor constraining the reliability of metal oxide chemi-resistors in critical application areas like environment monitoring, health diagnosis, automotive, space exploration, biomedical and pharmaceutical etc.

Raman spectroscopy is a reliable, sensitive and non-destructive method used in characterizing metal oxides and other nanomaterials [7, 8]. The Raman technique has been applied to study adsorption of molecules on the surface of metal oxides and to monitor their selective ability toward certain species of gas [9–11]. Among these studies, A_{1g} mode of SnO_2 was observed to show a huge enhancement when H_2S gas reacted with Cu doped SnO_2 nanomaterial [9]. This enhancement is observed to be absent when the material is exposed to air. The effect is reported to be reversible and the band is attributed to Cu_2S vibration, thus showing reactivity of Cu doped SnO_2 with H_2S . Nanocrystalline WO_3 powder has also been found to react with the reducing gases CH_4 and CO resulting in the growth of two broad band peaks at 1300 cm^{-1} and 1600 cm^{-1} which were observed to be absent in the Raman spectrum of pure WO_3 [10, 11]. Whereas, these peaks disappeared in the presence of an oxidizing gas NO_2 and thereby are attributed to the graphitic carbon peak usually present in many carbon materials [7]. This showed reactivity of CH_4 and CO with the WO_3 surface. Vanadium oxides materials are very sensitive to Raman spectroscopy [8, 12, 13] and are often characterized by it to explore their structural, metal-insulator and nanostructured properties [8]. The reason for this sensitivity is nothing less than the vanadium oxide's variation in its oxidation state and crystallographic structures which usually cause atomic or lattice displacement (distortion), causing active vibration [8, 12–18].

Vanadium pentoxide with a generic name (V_2O_5) and ionic state V^{5+} amidst other vanadium oxides (VO_2 , V_2O_3 , V_6O_{13} , V_3O_7 , etc) has been widely used for gas sensing due to its semiconductor and thermodynamic properties and atomic arrangement in the crystallographic unit cell [8, 12–18]. This material including VO_2 with V^{4+} ionic state, has been extensively applied for applications such as solar window, smart window; e.g. thermo-chromic and electrochromic devices, anti-reflecting coatings and lithium ion battery [12, 13, 17, 18]. V_2O_5 macroscopic structure (bulk), nano structure and the one whose radius is comparable with Debye length is thermodynamically favoured as orthorhombic unit cell at ambient conditions. This compound has the highest oxygen concentration among other vanadium oxide members; its crystallographic atomic arrangement provides room for corner-sharing and edge-sharing VO_6 octahedral geometry with space group D_{2h}^{13} $Pmnm$ (No. 59) layered structure and lattice parameters $a = 11.510\text{ \AA}$, $b = 3.563\text{ \AA}$ and $c = 4.369\text{ \AA}$ where b and c are frequently interchanged in orthorhombic system [17, 18]. According to the international crystallographic tables and density functional approximation records [17, 18], stoichiometric orthorhombic V_2O_5 structure should have four types of atoms in terms of their geometry coordination i.e. by their nature of bonding and bond length. One vanadium atom V and three different oxygen atoms O (1), O (2) and O (3) located

at different Wyckoff positions. V atom together with O (1) and O (3) occupy $4f$ Wyckoff position with site symmetry C_s whereas O (2) atom can occupy $2a$ Wyckoff position with site symmetry of C_{2v} [18, 19]. High symmetry orthorhombic lattice of V_2O_5 crystal structure with two formula per unit cell contains a total of 42 optical and acoustic modes. Among these 42 modes, three ground state modes are acoustic with zero frequency at high symmetry point called Γ -point.

The first order Raman active modes of this structure can be obtained from the symmetrized square of the vector representation (x, y, z) as the second rank polarizability tensor in the space group D_{2h}^{13} with 8 symmetry elements namely; E , $C_2(z)$, $C_2(y)$, $C_2(x)$, i , $\sigma(xy)$, $\sigma(xz)$ and $\sigma(yz)$ and by factor group analysis and selection rule for D_{2h}^1 point group. The infrared modes transform as (x, y, z) representation, since they are related to the electric dipole moment. Zhon *et al* [19] reported that 21 Raman active modes composed of A_g , B_{1g} , B_{2g} and B_{3g} modes may be presented in the V_2O_5 crystal while the remaining 18 modes may be due to infrared absorption (i.e. infrared active). On the other hand, the low temperature phase of VO_2 structures has space group $P2_1/(C_{2h}^5$ No. 14) and two atoms per unit cell in monoclinic crystal system. Group theory predicts 18 total modes and 15 optical zone-centre modes at wave vector $q = 0$ in the Brillouin zone (at Γ -point) from lattice mode representation by acting four symmetry elements E , $C_2(z)$, i and $\sigma(xy)$. These modes composed of A_{1g} , B_{1g} , B_{2g} and B_{3g} which were distributed in different configurations with respect to the crystal structure of the precursor compound. In this paper, we identify these vibrational modes in *in situ* Raman spectra of the V_2O_5 surface as it interacts with the NH_3 molecule as predicted from group theory. The study combined Raman spectroscopy methods, group theoretical approaches and electrophysical techniques to show the reactivity of vanadium oxide surface to NH_3 molecule at ambient temperatures and at $100\text{ }^\circ\text{C}$ by oxygen iono-sorption and lattice vibration mode assignment. The set-up could be miniaturized to find its usefulness in portable sensitive and selective chemical sensors or applied as a stationary industrial gas detector.

2. Theoretical considerations

This section includes some science of how Raman scattered photon population from a typical nanostructured surface is affected by the presence of reducing or oxidising gases. In this regard, one can use a number of basic theories providing the intensity, I , of Raman scattered photons as a function of surface characteristics. One of the most appropriate theories is the phonon confinement models generally given by [20–24].

$$I(\omega, q) = A_0 \int_0^\infty \frac{\exp(-\alpha q^2)}{[\omega - \omega(q)]^2 + (\Gamma_0/2)^2} dq \quad (1)$$

where q is the wave vector in the Brillouin zone, $\omega(q)$ is the phonon dispersion relation for the material, α is the scaling factor, Γ_0 is the full-width-at-half-maximum broadening of the Raman peak, and A_0 is the proportionality constant. The integral is performed over all ranges of the wave-vector, $q \sim 0$, which is further proportional to $\pi a/\lambda$, where λ is the

laser wavelength and a is the lattice parameter of the material. Any change in $I(\omega, q)$ should be due to less or more Raman scattered photons which means less or more phonons in the surface. This is a further signalling indicator of the chemical interactions or reactions that happen in presence of reducing or oxidising gases. The change in intensity of Raman scattered photons or phonons can be found by differentiating equation (1) with respect to both variables as follows

$$dI = A_0 \frac{\partial}{\partial \omega} \left(\int_0^\infty \frac{\exp(-\alpha q^2)}{[\omega - \omega(q)]^2 + (\Gamma_0/2)^2} dq \right) \Big|_q dq + A_0 \frac{\partial}{\partial q} \left(\int_0^\infty \frac{\exp(-\alpha q^2)}{[\omega - \omega(q)]^2 + (\Gamma_0/2)^2} dq \right) \Big|_\omega d\omega. \quad (2)$$

The first term in equation (2) gives the number of phonons of varying wavenumbers confined in the nano-particle but can only be evaluated numerically. The first part of equation (2) reduces to zero as a differential with respect to ω for the case when ω does not change, as will be seen in the experimental section this yields to null. The second term, however, can be simplified and equation (2) can then be re-written as

$$dI = A_0 \frac{[\exp(-\alpha q^2)]^2}{[\omega - \omega(q)]^2 + (\Gamma_0/2)^2} \left(\frac{2q\alpha [\exp(-\alpha q^2)]^2 [\omega - \omega(q)]^2 + (\Gamma_0/2)^2 + [\exp(-\alpha q^2)]^2 2 [\omega - \omega(q)] \frac{d\omega}{dq}}{[\omega - \omega(q)]^2 + (\Gamma_0/2)^2} \right). \quad (3)$$

In terms of the response defined from the changes in Raman peak heights and their changes, it is appropriate to evaluate the fractional change of intensity rather than merely change in intensity. The latter suffers from variations from spot to spot. Therefore, in this study we define Raman intensity response as a fractional change in intensity referenced to the Raman peak height before the analyte gas is introduced as follows:

$$\frac{dI}{I} = \frac{\frac{[\exp(-\alpha q^2)]^2}{[\omega - \omega(q)]^2 + (\Gamma_0/2)^2}}{\int_0^\infty \frac{\exp(-\alpha q^2)}{[\omega - \omega(q)]^2 + (\Gamma_0/2)^2} dq} \left(\frac{2q\alpha [\exp(-\alpha q^2)]^2 [\omega - \omega(q)]^2 + (\Gamma_0/2)^2 + [\exp(-\alpha q^2)]^2 2 [\omega - \omega(q)] \frac{d\omega}{dq}}{[\omega - \omega(q)]^2 + (\Gamma_0/2)^2} \right). \quad (4)$$

When equation (4) is further analysed in terms of the actual sensing, one can reduce it to the following shorthand version:

$$\frac{dI}{I} = f(q, \omega(q), \omega, \alpha). \quad (5)$$

Since λ is a laser wavelength, which is a constant during the Raman spectra acquisition and $q = 2\pi/\lambda$, then q is a constant and $\omega(q)$ is constant. We shall show in the experimental section that ω is also a constant. Therefore we can re-write it to

$$\frac{dI}{I} = f(\alpha). \quad (6)$$

The scaling factor α varies from materials surface to another and also depends on polarization effects apart from the number of phonons interacting with the laser photons. The number of phonons is further affected by the presence of gaseous molecules. This theoretical discussion on Raman peak intensity changes will be discussed further with experimental validation in later section.

It is also very important to discuss the theory of phonon frequency (wavenumber) changes owing to gas interaction with the material surface. There will be blue or red shifts in the vibrational frequencies due to these changes. If one imagines a linear chain model of fundamental frequency $\omega^2 = \kappa/\mu$, where κ and μ are spring constant and reduced mass of the masses on the spring, respectively, then the change in vibrational frequency, $d\omega$, should be one that depends on both the change in μ and κ . The change in κ takes place when the number of electrons per bond change, whereas the change in μ happens when active gas elements such as oxygen desorbs or adsorbs. These changes can be, mathematically, represented as follows:

$$\frac{\partial \omega}{\partial \kappa} = \frac{1}{2\sqrt{\kappa/\mu}} \quad (7)$$

and

$$\frac{\partial \omega}{\partial \mu} = \left(-\frac{\kappa}{\mu^2} \right) \frac{1}{2\sqrt{\kappa/\mu}} = \left(-\frac{\kappa}{\mu^2} \right) \frac{\partial \omega}{\partial \kappa}. \quad (8)$$

The total change in frequency can be written as

$$d\omega = \frac{\partial \omega}{\partial \mu} d\mu + \frac{\partial \omega}{\partial \kappa} d\kappa = \frac{1}{2\sqrt{\kappa/\mu}} \left(d\kappa - \frac{\kappa}{\mu^2} d\mu \right). \quad (9)$$

So, if $d\kappa > d\mu/\mu^2$, one expects a blue shift, whereas when $d\kappa < d\mu/\mu^2$ then one should expect a redshift in the Raman spectra. Both change in intensity of the phonon (equations (1)–(3)) and their frequencies (equations (4)–(6)) will be used to explain the *in situ* Raman spectra with gas sensing.

3. Experimental

A pulse laser deposition (PLD) technique was employed in this study to grow VO_x thin film on Corning glass substrates. The glass substrates were rigorously cleaned and rinsed several times (in ethanol and deionized water) with an ultrasonic bath in order to remove impurities and ensure quality. Vanadium oxide (VO_2 nanoparticles (NPs) powder with 99.9% purity) from Sigma Aldrich was converted to pellet using an

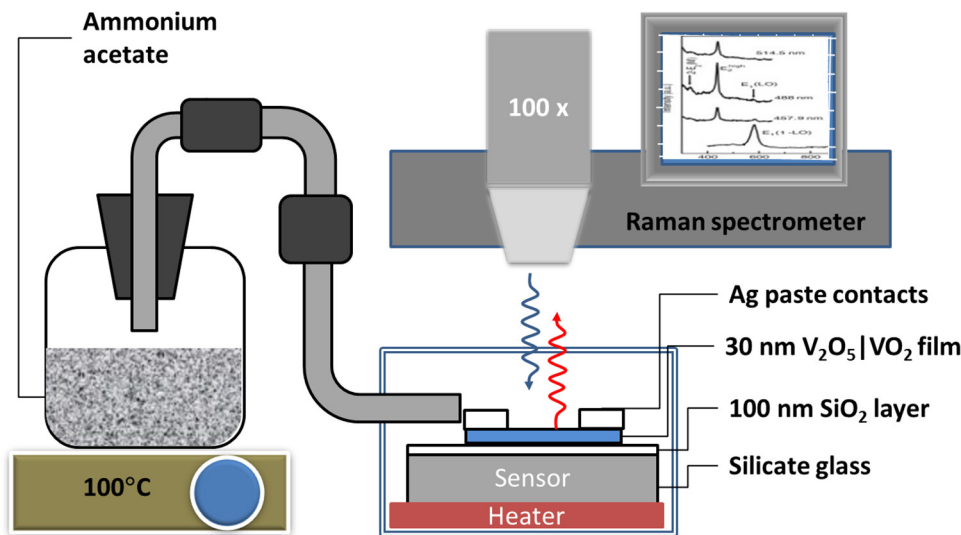


Figure 1. Schematic diagram of the *in situ* Raman measurement illustrating how the NH₃ gas sensing measurement was performed on the V₂O₅ surface.

ENERPAC P142 hydraulic cold press system made in the USA. About 5 g of VO₂ (NPs) powder was slightly dampened with methanol and transferred into a 20 mm hollow die after which a load of 100 tons was mounted on the specimen, and the resulting pellet was annealed at 500° C for ~24 h. The set-up and plasma plume dynamics of the PLD system used for this work is similar to the one reported in [25]. Nd:YAG laser beam ($\lambda = 266$ nm, $\tau = 8$ ns) was directed to the chamber by the aid of several mirrors and later focused onto the VO₂ pellet target at an incident angle of 45° using two cylindrical lenses. The minimum pulse energy was applied at 45 mJ with laser fluence of 2 J cm⁻¹ and the substrate to target distance of 5 cm was maintained during deposition. Oxygen partial pressure was set to 0.05 mbar (37 mTorr) after evacuating the chamber to the base pressure of 3.1×10^{-5} mbar, and the film was deposited for 30 min. The x-ray diffraction patterns of the film were measured at room temperature using the Panalytical XPERT PRO PW3050/50 diffractometer with CuK α radiation (45 kV, 400 mA, $\lambda = 0.1540598$ nm and $5^\circ \leq 2\theta \leq 90^\circ$). The Auriga ZEISS scanning electron microscope (SEM) was employed to study the morphology of the film and to estimate the thickness of oxide layers that are present. SAXSess Anton Paar small-angle x-ray scattering spectroscopy was employed for the particle size and pore size analysis of the film. High resolution x-ray photoelectron spectroscopy (XPS) was obtained with a PHI 5000 Versaprobe system. A low energy Ar⁺ ion gun and low energy neutralizer electron gun were used to minimize charging on the surface. A 100 μ m diameter monochromatic Al K α x-ray beam ($h\nu = 1486.6$ eV) generated by a 25 W, 15 kV electron beam was used to analyze the different binding energy peaks. The pass energy was set to 11 eV giving an analyzer resolution ≤ 0.5 eV. Multipack version 8.2 software was utilized to analyze the spectra to identify the chemical compounds and their electronic states using Gaussian–Lorentz fits.

Time of flight secondary ion mass spectroscopy (TOF-SIMS) analyses were performed using an IONTOF TOF SIMS⁵ instrument with bismuth 1+ as the primary ion source (30 kV, 1 pA pulsed at 10 kHz). These analyses were carried out

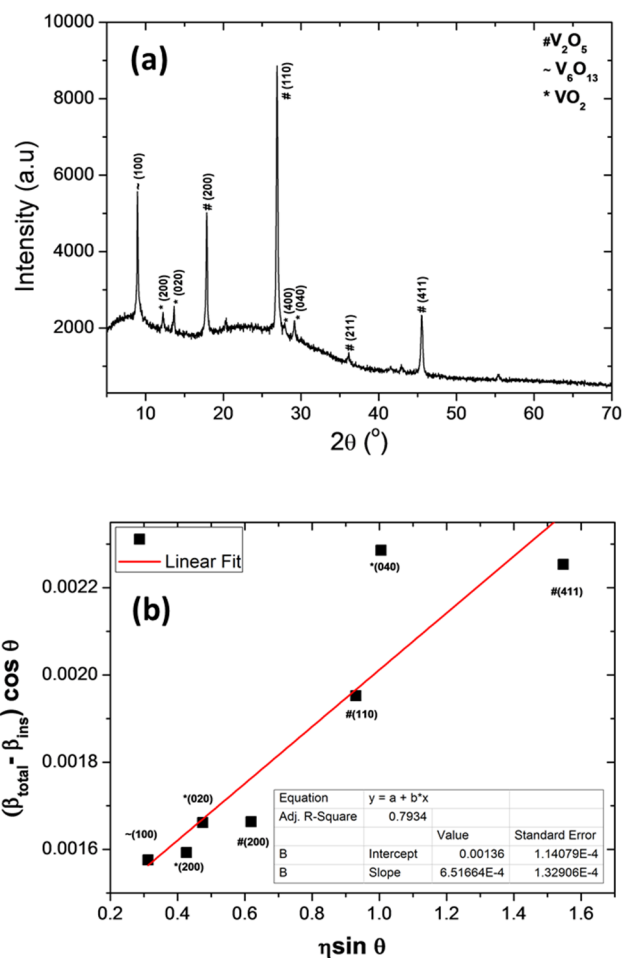


Figure 2. (a) XRD pattern of V₂O₅ film, (b) Williamson–Hull plot for the grains stain determination.

in negative secondary ion mode and under ultra-high vacuum (base pressure) of $\sim 10^{-9}$ mbar. A Cesium (1 kV, 75 nA) sputter gun was used. The analysis area was 100 \times 100 μ m² and the sputter area was 300 \times 300 μ m² at a resolution of 512 \times 512 pixels with a binning of 4 pixels.

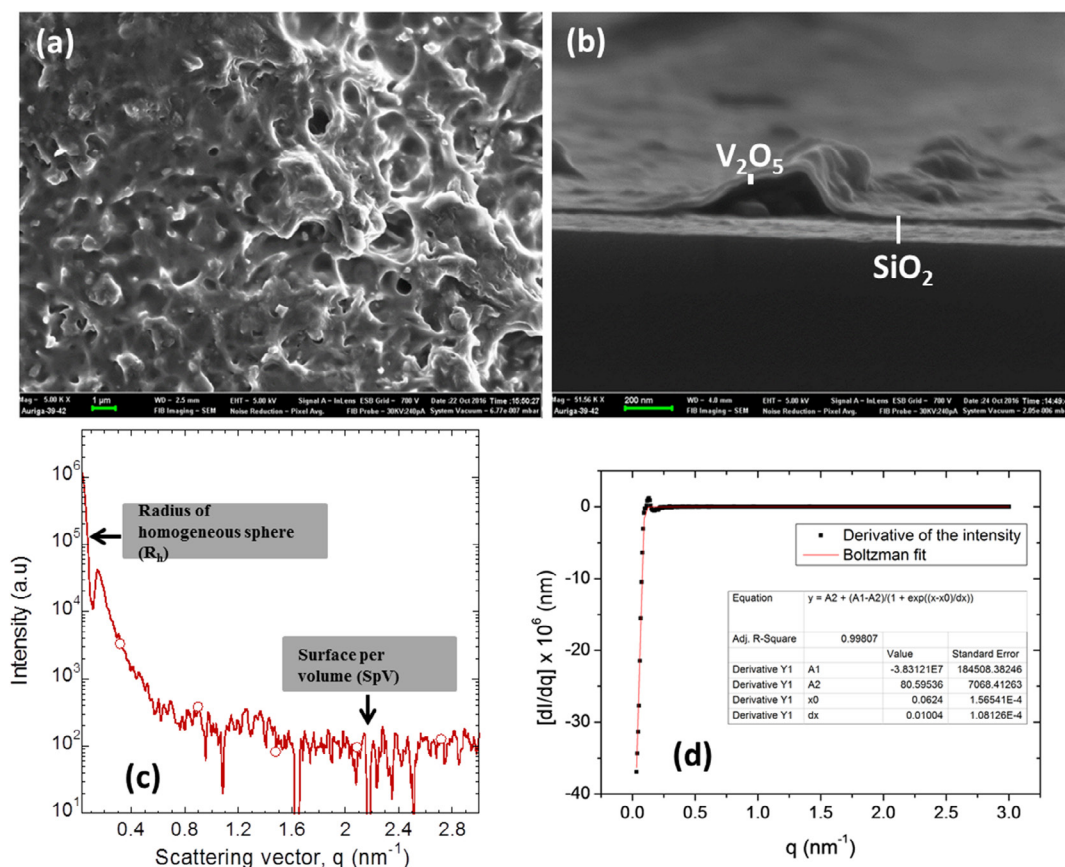


Figure 3. SEM images and SAXS spectrum of V_2O_5 film, (a) in-plane surface image, (b) cross-section image at the edge of the film showing three distinct layers, (c) SAXS analysis showing regions where the average radius of homogeneous spheres and surface per volume are extrapolated from, (d) the differential of the (I, q) data with respect to q .

Raman structural properties of the film and *in situ*-sensing measurement of NH_3 effluent produced from ammonium acetate at $100\text{ }^\circ\text{C}$ was carried out using a Bruker spectrometer. A Bruker Raman Senterra spectrometer equipped with $50\times$ optical objective and a 532 nm excitation laser, at a laser power of 0.2 mW , was used for accumulating the films' spectra. The typical experimental set-up of the *in situ* Raman sensing measurement is presented in figure 1 wherein a 532 nm Nd:YAG laser was directed to the film glued onto an Al_2O_3 -Pt interdigitated electrode set. The heating terminals of the interdigitated electrode are connected to a DC power supply and the whole specimen is enclosed in a transparent chamber where NH_3 effluent from the thermal decomposition of ammonium acetate was allowed flow through. Conductometric sensing measurements were conducted using KSGA565 KENOSISTEC sensing station set-up from Italy. The film surface was wire bonded by silver paste in two terminals configurations to allow connection with the KSGA565-KEITHLEY source meter, after which the currents across the film were measured for different concentrations of NH_3 gas.

4. Results and discussion

Figure 2(a) shows the XRD pattern of the film, the pattern shows that the film is predominantly composed of V_2O_5 , according to the Institute for crystallographic and diffraction database, with a powder diffraction number of (PDF 41-1426)

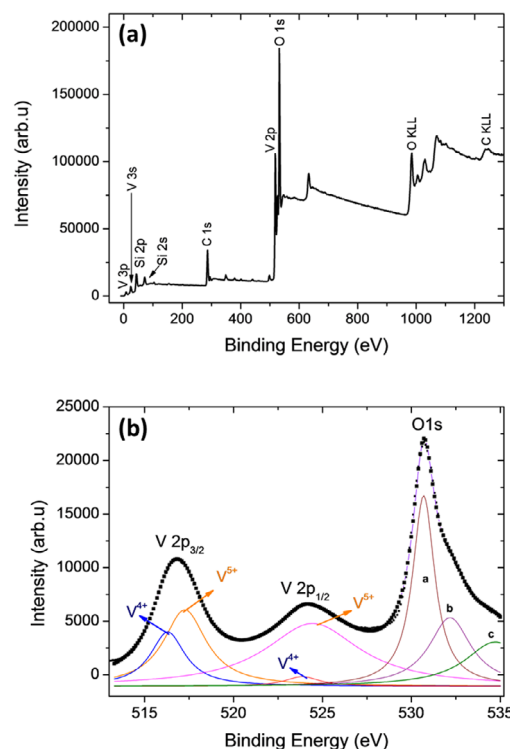


Figure 4. XPS spectra of the V_2O_5 film, (a) broad survey scan spectrum, (b) higher resolution deconvoluted core level spectrum of V-2p and O-1s for the V_2O_5 film.

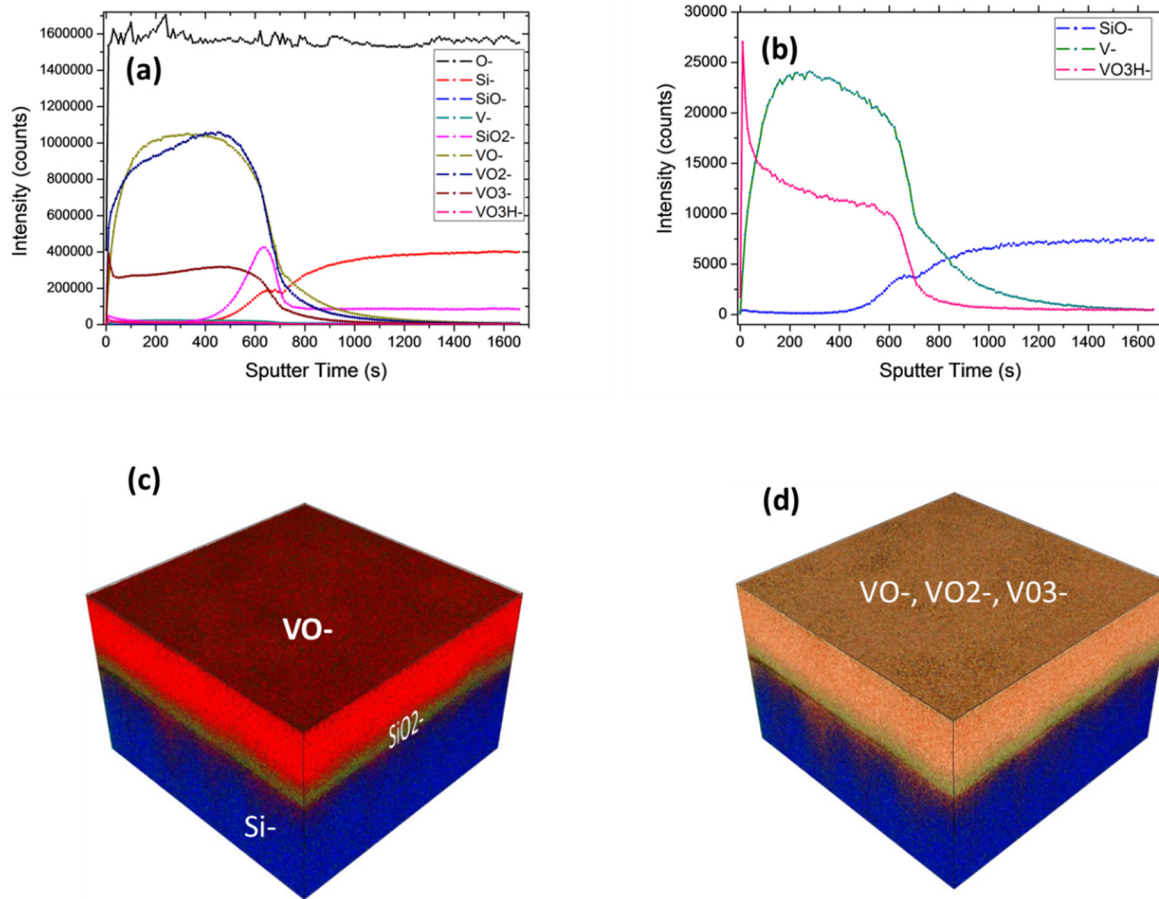


Figure 5. (a) TOF-SIMS depth profile of the negative ions of V, VO, Si and SiO species available in the film, (b) is the TOF-SIMS depth profile spectrum showing the low counts SiO-, V- and VO3H- species in (a), (c) 3D overlays image of the ions of the film consisting of Si-, SiO₂- and VO, (d) 3D overlays image of the entire film displaying VO-, VO₂- and VO₃- as the surface ions.

but with trace phases of VO₂ and V₆O₁₃ according to (PDF 76-0676) and (PDF 27-1318), respectively. This x-ray spectrum has been matched with the Rietveld structure refinement method with the Bragg positions showing strong correlation with the V₂O₅ structure; this report is given in the supplementary material (SM) (stacks.iop.org/JPhysD/51/015106/mmedia). The average crystallite size *L* and lattice micro/nano strain ϵ of the film were calculated using the well-known Scherrer's and Williamson–Hall formula (presented in the SM) [26, 27] and were found to be ~70nm and $0.000651 \pm 1.32 \times 10^{-4}$, respectively. Figure 2(b) is the plot of the Williamson–Hall assumption for lattice strain determination. The film morphology are presented in figure 3 with (a) showing the in-plane formation of clusters of particles with pores at the surface and (b) the cross section at the edge of the film showing that the film is ~30nm in thickness. Figure 3(c) presents a small-angle-x-ray-scattering (SAXS) plot of scattering intensity versus the wave vector for the V₂O₅ layer. From the software on the SAXS instrument based on Guinier *et al*'s formulations, the morphology of the layer is interpreted to be composed of nearly spherical particles from the linearity of the extreme side of the small wave vector and this gives a mean particle diameter of 51.15 ± 0.60 nm. This translates to a surface-to-volume ratio estimated at 8.25 ± 628.60

$\text{m}^2 \text{cm}^{-3}$ estimated at the wave vector of 2nm^{-1} end of the spectrum. Figure 3(d) presents a differential of the spectrum in figure 3(c) which is derived from the well know intensity–wave vector–radial distance equation [28]

$$I = c \int_0^\infty n(r) f(q, r) S(q, r) dr \quad (10)$$

where $n(r)$ is the normal particle size distribution curve such as the Gaussian, Loretzian or lognormal and the like, $f(q, r)$ is the form factor and $S(q, r)$ is the structure factor. For materials without dopants like in our present case, the form factor is unity and similarly the structure factor. Therefore, a differential of the (q, I) data with respect to q of equation (10) gives a plot of the S -curve type as given in figure 3(d). When a Boltzmann's S -curve equation is fitted to the differential curve, the central q_0 and its standard deviation are found to be $0.06 \pm 1.58 \times 10^{-4}$ which when converted from the reciprocal space, q , to the real space, r , gives the mean diameter, r_0 , of about 50nm which confirms the software-obtained value of the particle size. We can conclude the average particle size by SAXS to be 51 nm for this 30nm layer which, when hexagonal close packing of these particles is considered, forms pores of mean diameter of about 20nm. Phonon confinement is therefore possible because of the tight pore size rather than particle size.

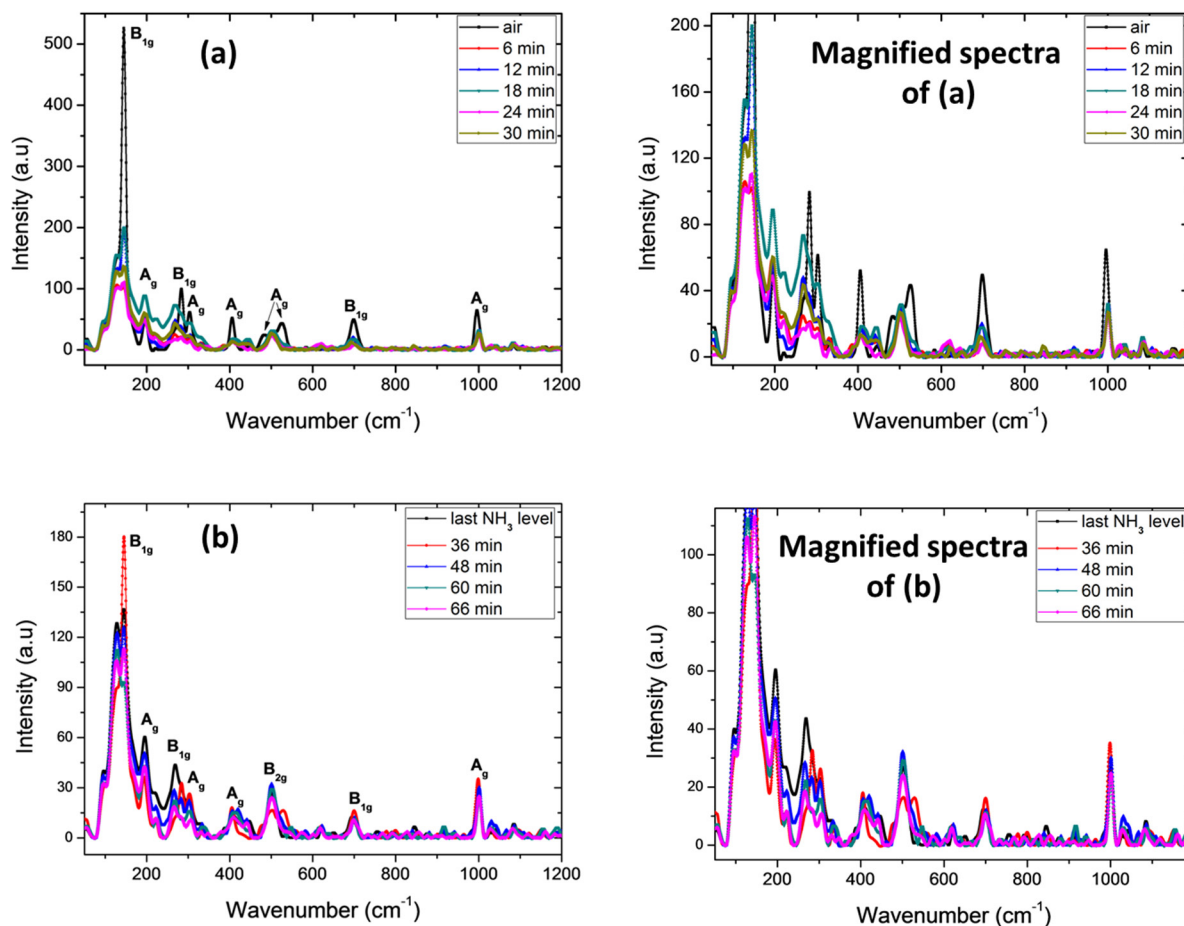


Figure 6. (a) Raman spectra at 25 °C of V_2O_5 film in air, and covered with NH_3 molecule recorded at 6 min intervals, (b) Raman spectra at 25 °C of V_2O_5 film recovering from NH_3 molecule recorded at 6 and 12 min intervals.

XPS spectrum of the surface of the V_2O_5 film is represented in figure 4 with (a) displaying the overall core level XPS survey spectrum and (b) showing Lorentzian–Gaussian deconvoluted core level spectrum of V-2p and O-1s for the V_2O_5 film. The $\frac{1}{2}$ spin–orbit doublet component of the V-2p photoelectron was found to be 524.9 eV for V^{5+} and 523.6 eV for V^{4+} state while the $\frac{3}{2}$ spin–orbit component after further Lorentzian–Gaussian dividing peak analysis gives 517.25 and 516.2 eV for V^{5+} and V^{4+} respectively [29, 30]. The oxygen O1s is deconvoluted into three peaks, 531, 533 and 535 eV which can be assigned to adsorbed oxygen (a), single bonded oxygen (b) and double bonded oxygen (c) respectively. The TOF SIMS measurement has been used to unveil the chemical elements that are present in V_2O_5 film as a function of sputter-depth, the results are presented in figure 5 where (a) shows depth profile of the negative ions of V, VO, Si and SiO species, (b) is the magnified spectrum of SiO-, V- and VO3H-species and (c) and (d) are the overlay images of all the compounds present in the film. The spectra of ions with depth in figure 5(a) and their image overlays in figure 5(c) shows that vanadium oxides species dominate the film surface to ~500 s sputter time. This analysis is in good agreement with the above XPS results in that VO_2 (V^{4+}) and V_2O_5 (V^{5+}) were seen to be more at the surface. This is also true for XRD analysis that shows diffraction peaks for VO_2 (V^{4+}), V_2O_5 (V^{5+})

and V_6O_{13} which happen to be V^{4+} and V^{5+} mixed oxide. The TOF-SIMS spectrum in figure 5(a) and overlays images in figure 5(c) also made it possible to understand the V_2O_5 film layers in the SEM cross-section image in figure 3(b) and estimate the film thickness. It was found that in ~500 s sputter time ~30 nm vanadium oxides layer was sputtered completely and thereafter the gun penetrated into the interface region in ~700 s sputter time which is found to be rich in SiO_2 . This SiO_2 layer has been estimated to be ~100 nm from the cross-section SEM image.

4.1. In situ Raman spectroscopy with gas sensing at 25 °C

Figure 6 shows the effect of atmosphere changes in the surface of V_2O_5 film when subjected to the effluent of NH_3 from the compound of ammonium acetate. Figure 6(a) illustrates the change in Raman spectra of the film when exposed to the molecule at different times (with intervals of 6 min) and to air (as a control spectrum) at 25 °C, while figure 6(b) represents the change in the Raman spectrum of the film when recovering from NH_3 . In these profiles, the authors observed that the modes at low-frequency Raman line region of V_2O_5 , earlier classified as rigid-layer modes [13] with bending vibration characteristics, were mostly unaltered in wavenumber when the film was subjected to the NH_3 effluent. Interestingly, the

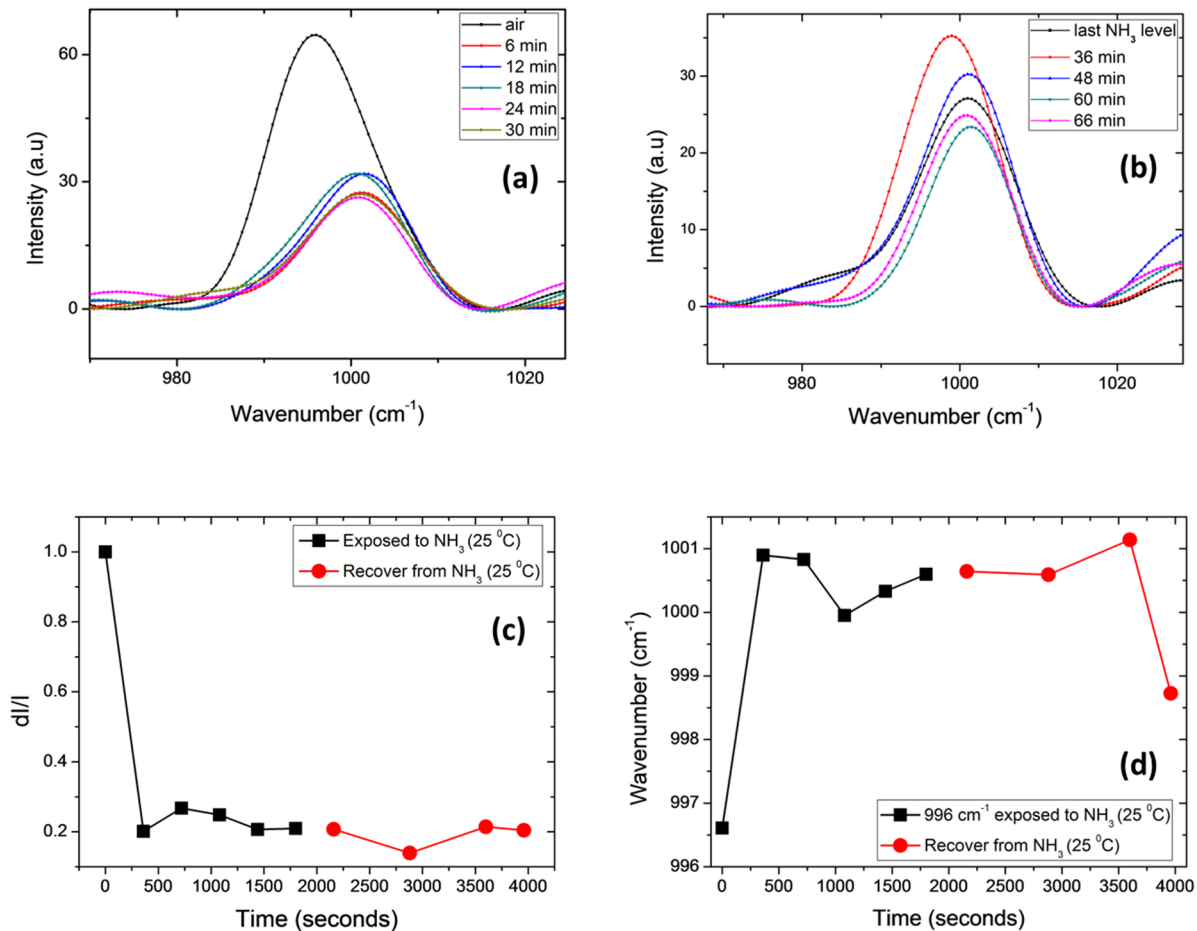


Figure 7. (a) Magnified images of 996 cm^{-1} Raman lines when the film is exposed to NH_3 at 25°C , (b) magnified images of 996 cm^{-1} Raman lines when the film is recovering from NH_3 at 25°C , (c) Gaussian fitted data of the heights of low-frequencies 143 cm^{-1} Raman lines when the film is exposed to and recovering from NH_3 at 25°C , (d) Gaussian fitted data of peak-positions of high-frequencies 996 cm^{-1} Raman lines when the film is exposed to and recovering from NH_3 at 25°C .

one at 194 cm^{-1} which shows a shift to low-frequency Raman line was observed to redshift. On the other hand, at the higher-frequency side of the Raman spectra, the 996 cm^{-1} stretching mode displayed significant shift towards high frequency of the Raman line (blueshift) in all spectra (shown in figure 7(a)). The reverse effect was observed when recovering the film from effluent of NH_3 in figures 6(b) and 7(b), where both blueshifted 996 cm^{-1} and redshifted 194 cm^{-1} modes showed some recovery potential.

In accordance with equation (6) where the change in Raman line position $d\omega$, as a function of both elastic constant of the bonds, κ , and reduced mass of the atoms around these bonds, μ , is given by $d\omega \propto d\kappa - (\kappa/\mu^2)d\mu$. In the present system case: $1/\mu = (1/m_O) + (1/m_V)$ or $\mu = m_O m_V / (m_O + m_V)$. The increase in κ could be ascribed to acceptance of an electron by the V_2O_5 surface from the NH_3 effluent and vice versa, whereas an increase in μ could be ascribed to the acceptance of atoms from the gas by the V_2O_5 surface. Changes in κ should be prevalent at 25°C where adsorption is more likely to happen, while an increase in μ is likely to happen at high temperatures where chemisorption due to breakage of NH_3 bonds is preferred.

Since the 996 cm^{-1} phonon is being blue-shifted [i.e. $d\omega > 0$] when exposed to NH_3 , one expects that $d\kappa > d\mu/\mu^2$. This means that the change in elastic κ is larger than the

change in μ . This suggests that V–O bond gains electrons from NH_3 . On the other hand, the observation that the 194 cm^{-1} phonon is being red-shifted when NH_3 is introduced means that $d\kappa < d\mu/\mu^2$. This could indicate that the V–O–V or O–V–O bonds prevalent in the VO_2 system are losing electrons to the NH_3 at 25°C . This surprising result leads to the conclusion that bonds that have many electrons tend to gain more electrons whereas those bonds that have less electrons tend to lose even the few electrons that they have. This phenomenon is similar to an observation made during the halogenation of organic alkanes with HCl or HF or HBr in 1890s by a scientist known as Markovnikov, who observed that the H atom preferred to attach itself to carbon with the highest number of H atoms [31, 32].

A decrease in intensities of 145 cm^{-1} low-frequency Raman line of V_2O_5 were also observed as a function of NH_3 effluent exposure (figure 6(a)) [33], but a reverse effect is observed when recovering the surface from NH_3 exposure in that the intensities increased slowly and saturate (figure 6(b)) with less potential when recovering from the NH_3 effluent. The profiles in figures 7(c) and (d) are representative of the change in intensity (dI/I) of the 145 cm^{-1} Raman lines and wavenumber (ω) peak-positions of 996 cm^{-1} Raman line at 25°C . These line profiles show that the intensities of 145 cm^{-1} phonon

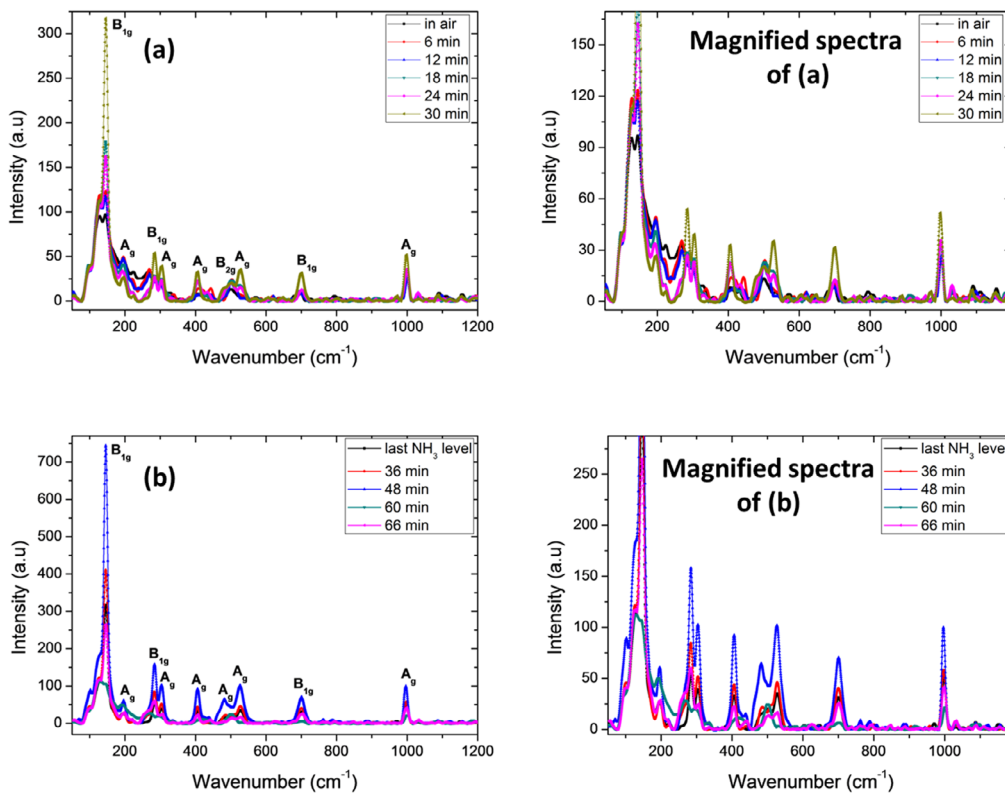


Figure 8. (a) Raman spectra at 100 °C of V₂O₅ film in air, and covered with NH₃ molecule recorded at 6 min intervals, (b) Raman spectra at 100 °C of V₂O₅ film recovering from NH₃ molecule recorded at 6 and 12 min intervals.

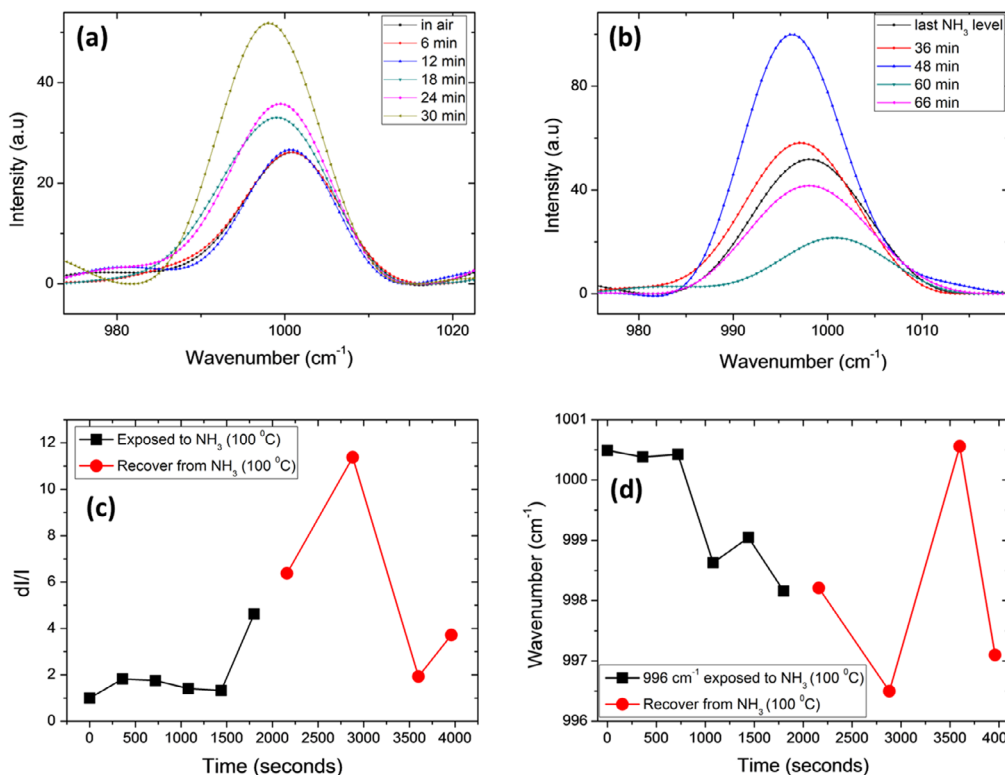


Figure 9. (a) Magnified images of 996 cm⁻¹ Raman lines when the film is exposed to NH₃ at 100 °C, (b) magnified images of 996 cm⁻¹ Raman lines when the film is recovering from NH₃ at 100 °C, (c) Gaussian fitted data of the heights of low-frequencies 143 cm⁻¹ Raman lines when the film is exposed to and recovering from NH₃ at 100 °C, (d) Gaussian fitted data of peak-positions of high-frequencies 996 cm⁻¹ Raman lines when the film is exposed to and recovering from NH₃ at 100 °C.

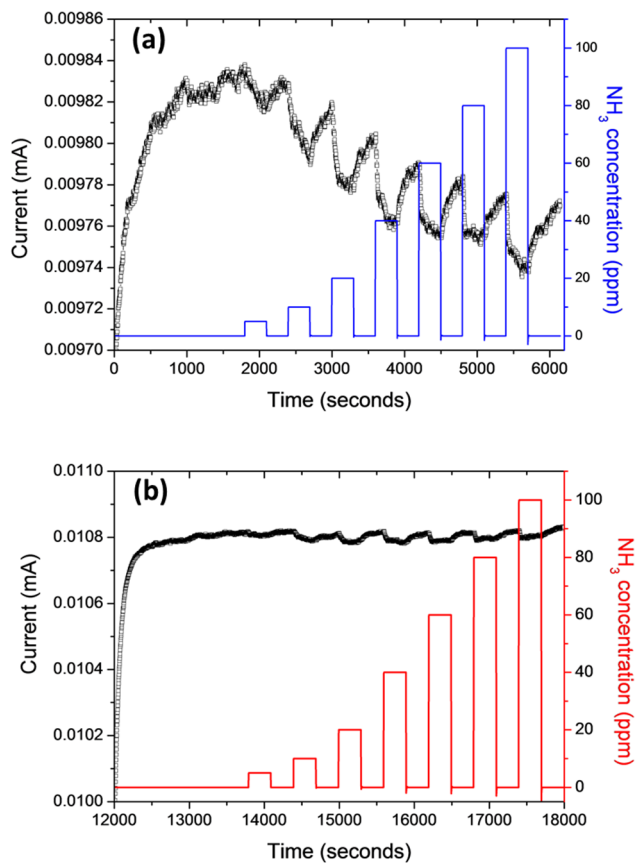


Figure 10. Conductometric sensing signal for NH₃, (a) at room temperature, (b) at 100 °C.

decrease and saturate with time during exposure, and experience difficulty in recovery due to the lack of vents in the home made gas sensing cell shown in figure 1. This decrease in Raman scattered intensities in the presence of molecules may also be due to the absorption of laser light of free electrons created as a result of the interaction between V₂O₅ and NH₃ [10]. The Raman fingerprint position of 996 cm⁻¹ phonon recorded more significant blueshift (4 cm⁻¹) before saturation when exposed to the NH₃ molecule with relatively high potential of recovery than the redshift of the 194 cm⁻¹ (2 cm⁻¹) as shown in figure 7(d).

4.2. In situ Raman spectroscopy with gas sensing at 100 °C

In the same manner, figure 8(a) displays the Raman spectra of the film when exposed to the effluent of the NH₃ molecule at different times (with interval of 6 min) and to air (as control spectrum) at 100 °C, while figure 8(b) shows the change in Raman spectra of the film when recovering from the molecule. Figures 9(a) and (b) are the magnified spectra of 996 cm⁻¹ Raman lines when the surface is exposed to and recovering from NH₃ at 100 °C while the profiles in figures 9(c) and (d) are the change in intensity (dI/I) of 145 cm⁻¹ Raman line and wavenumber peak-position of 996 cm⁻¹ at 100 °C. The fact that the phonons are thermally mediated, coupled with the possibility of less scattering of light at the less-dense environment, may be responsible for the change observed at 100 °C relative to the effects observed in the case of room temperature measurements (25 °C). It is true that the way and manner

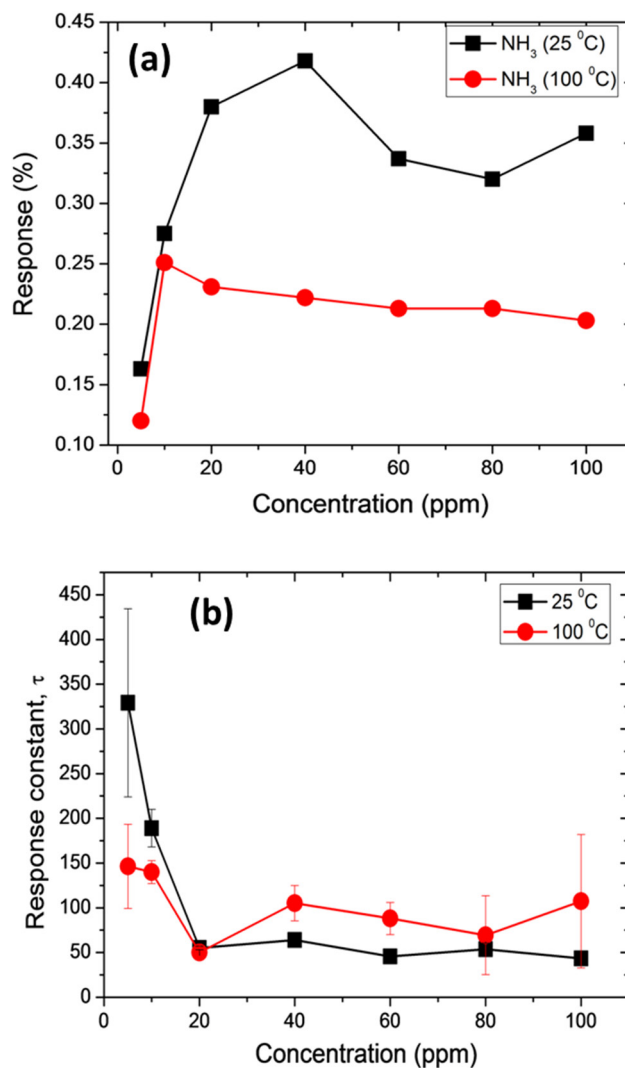


Figure 11. (a) Response curve as a function of different NH₃ gas concentrations, (b) plot of the response time constant for different concentrations of NH₃ gas.

in which the NH₃ molecule sits on the V₂O₅ will greatly influence the charge distribution between them [24]. In addition to the V₂O₅ crystal, geometrical structure and space group discussed in the introduction, V₂O₅ is a layered structure having distorted square pyramids of VO₅ which share edges and corners with the apex of the V–O configuration having a much shorter bond length compared to other bonds. This short bond length corresponds to a double bond attachment [17, 34]. One may propose that hydrogen atoms in an NH₃ molecule in a trigonal pyramid structure preferred to attach themselves to the vanadyl oxygen (i.e the one with double bond and shorter length). If so, that may cause the molecule to give away some of their charges to the V = O layer and consequently increase the spring constant which leads to a blueshift in the Raman spectrum. Thus, the remnants of the NH₃ dissociation that are lying in the chamber may regroup and attach themselves to the bonded hydrogen atom and revert back to the NH₃ molecule when recovering V₂O₅ film from the coverage.

Other Raman frequency modes of V₂O₅ observed were 225, 270, 283, 305, 335, 406, 503, 614 and 700 cm⁻¹ at 25 °C and 100 °C, and they all belong to the vibration

Table 1. Summary of Raman signatures versus chemi-resistive sensing of NH₃ molecule at the V₂O₅ surface.

Sensing properties due to Raman signatures			
Temp °C	Derivative (dI/I) of 143 cm ⁻¹		Change in wavenumber ($\Delta\omega$) of 996 cm ⁻¹
	Response	Response τ (s)	Response
25	-0.799	300	4
100	3.6	1400	-3.2
Sensing properties due to Chemi-resistive test			
Temp °C	Chemi-resistive at 40 ppm		
	Response	Response τ (s)	
25	0.419	59	
100	0.222	105	

modes of V₂O₅ except the modes at 194 cm⁻¹ and 614 cm⁻¹ which are Raman fingerprint positions for the VO₂ structure [13, 19, 26, 35, 36]; this shows that VO₂ crystallites are not participating in the reactivity of NH₃ effluent molecule.

4.3. Comparison of *in situ* Raman spectroscopy-gas-sensor tester and the traditional chemi-resistive gas-sensor testing station

Figure 10 shows electrical measurements of the V₂O₅ film in the presence and absence of NH₃ gas via the set-up described in the experimental section and previously reported [14, 37]. Figure 10(a) is the transient time-conductometric signals of the film when exposed to NH₃ gas at room (25 °C) and figure 10(b) is the signals at 100 °C. The profile shows a decrease in conduction of the film in the presence of NH₃ gas at 25 °C and 100 °C for every concentration. The sensor response and response time constant calculations for different concentrations of NH₃ gas are given as follows:

$$\frac{i}{i_0} = \exp \frac{t}{\tau_1} \quad 0 \leq t \leq t_1 \quad (11)$$

$$\frac{i}{i_0} = \exp \frac{t}{\tau_1} \times \exp \frac{t-t_1}{\tau_2} \quad t_1 < t \leq t_2 \quad (12)$$

where i_0 is the initial current of the sensor in synthetic air (flowing through the chamber), t_1 is the time for i_0 value, i is either the current when the target gas is turned on or off and t_2 is the time at which the sensor recover to its original value. The quantity τ_1 and τ_2 are the time constants for response and recovery steps, these parameters were calculated by fitting the first order exponential function in equations (11) and (12). Figure 11(a) shows a response profile which was calculated from equation (11). The pattern shows better adsorption for all concentrations of the NH₃ gas at 25 °C compared to the one at 100 °C. A response time constant plot was extracted from the same equation(11) as shown in figure 11(b). The response time constant in this paper is defined as the time it takes the sensor to reach 63% i.e $1 - e^{-1}$ of its maximum after exposed to the gas [15, 38, 39]. This result also showed that the responses at 25 °C are faster than that of 100 °C but responses at 100 °C showed stability compared with ones at 25 °C. There is a cross-over in the response time at 20 ppm where the response time is found to be 50 s.

When one compares both the *in situ* Raman spectroscopy gas sensor tester and the traditional conductometric sensing as summerized in the table 1 below, firstly one can infer that at 25 °C the change in the wavenumber of 996 cm⁻¹ (with + shift or blue shift of 4 cm⁻¹) is greater than at 100 °C (with - shift or red shif of 3.2 cm⁻¹) and that the two temperatures showed significant and comparable recovery. On the other hand, the response according to the fractional change in intensity at 25 °C is great (with downward turn or -0.799) compared with the 0.419 of the chemi-resistive test and the one at 100 °C (with upward turn or +3.6) is large compared with the 0.222 of the chemiresistive test. This showed that the *in situ* Raman spectroscopy gas-sensor tester is more responsive than the chemi-resistive sensor especially when considering the fact that the NH₃ effluent concentration in the chamber may be less or even far less than 40 ppm. Also, when one compares the two response time constants, the chemi-resistive sensor showed faster response compared with the *in situ* Raman spectroscopy gas sensor-tester. Again a low concentration of the effluent NH₃ in the *in situ* Raman gas sensing chamber may be the cause. This study shows that apart from using the response due to the fractional change in Raman intensity and chemi-resistive signal, Raman wavenumber (frequency) shift can be employed to selectively monitor gas leakages in the environment or to monitor decomposition of gases in industry during gas processing.

5. Conclusions

In summary, *in situ* Raman spectroscopy has been employed to monitor the reactivity of NH₃ effluence produced from ammonium acetate salt decomposed at 100 °C at the surface of 30 nm layers (with spherical particle of ~51 nm and pores of ~20 nm) of V₂O₅ film deposited by PLD techniques. The results showed a recoverable red shift in the 194 cm⁻¹ phonons and blue shift in the 996 cm⁻¹ phonons upon the interaction of the molecule at ambient temperature (25 °C) and 100 °C. Adsorption effects (increase in intensity) of 145 cm⁻¹ phonons were also observed at these two temperatures. The Raman scattered adsorption effect has been explained using phonon confinement models by taking fractional change in intensity into account while the blue or red shift in the wavenumber (frequency) is related to the change in elastic constant and the reduced mass of the sensing surface *in situ* with NH₃ ambience. The adsorption effect is related to more and/or less Raman scattered photons

while frequency shift is explained as a decrease in the elastic constant (acceptance of charges from the molecule) when blue shifted and decrease in elastic constant (donation of charges) or increase in reduced mass (chemisorption) when red shifted. Acceptance of charges by the V_2O_5 surface from the molecule is observed to be prevalent at the ambient temperature while an increase in the reduced mass is observed at 100 °C. This is considered to be true since the breaking of chemical bonds or decomposition of NH_3 could only take place at a temperature higher than that of the ambient temperature.

Comparison and rankings of *in situ* Raman spectroscopy gas-sensor tester with the traditional chemi-resistive sensor tester showed that the *in situ* Raman spectroscopy sensor tester is excellent. Additionally, the significant recoverable blue shift and red shift observed when NH_3 interacts with the surface may be considered an outstanding feature of *in situ* Raman spectroscopy on selective monitoring of gas leakage in the environment or to monitor decomposition in industry during gas processing. Hopefully the technique will be helpful in advancing or upgrading the design of chemical sensors for environmental or industrial pollution monitoring.

6. Future plans

The effect of electron capture from the V–O–V bond and the same being donated to the V = O bonds can also be seen with XPS. This can be accomplished through (1) analysis of XPS spectra or (2) *in situ* XPS with NH_3 gas injection. In (1) the analysis through peak deconvolution shows several chemical states of vanadium: V^{4+} and V^{5+} and oxygen: O_2^- or O_1s but that the three oxygen peaks (about 531, 533 and 535 eV) can be assigned to adsorbed oxygen (a), single bonded oxygen (b) and double bonded oxygen (c), respectively. It is more likely that upon NH_3 injection, the NH_3 and adsorbed oxygen interaction gives electrons to the double bond with a higher probability than to a single bond in the V_2O_5 chemical structure. This XPS explanation concurs very well with the experimental observation from our current Raman spectroscopy where we observe a relaxation of the V–O–V bond leading to red-shift in the peak and the stiffening of the V = O bond which shows a blue shift. As for (2), in order to verify the analysis in (1), there is a need to perform *in situ* XPS with a few ppm's of NH_3 in the XPS chamber and monitoring the evolution of the V and O peaks. To perform such an experiment, one would need to incorporate a gas chamber to the XPS set-up. Currently we do not have XPS facility in our laboratory; the XPS data included in this manuscript was acquired from another institute.

Acknowledgments

A A Akande acknowledges CSIR National Centre for Nano-Structured Materials for PhD Studentship position (project number HGER27S and HGER50S) and the National Research Foundation through KIC150917142805 travel grant. He also acknowledges the assistance of Bafana Moya of National Laser Centre during PLD experiments and Egger Sharon of National Centre for Nano-Structured Materials Characterization Facility for SEM Cross section.

ORCID iDs

Amos Adeleke Akande  <https://orcid.org/0000-0002-3691-9233>

References

- [1] Seiyama T and Kato A 1962 A new detector for gaseous components using semiconductive thin films *Anal. Chem.* **34** 1502
- [2] Brattain W H and Bardeen J 1953 Surface properties of germanium *Bell Syst. Tech. J.* **32** 1–41
- [3] Neri G 2015 Fifty years of chemoresistive gas sensors *Chemosensors* **3** 1–20
- [4] Kasalizadeh M, Khodadadi A A and Mortazavi Y 2013 Coupled metal oxide-doped Pt/SnO₂ semiconductor and yttria-stabilized zirconia electrochemical sensors for detection of VOCs *J. Elec. Soc.* **1160** B218–24
- [5] Lee Y W, Kim E, Shin B and Lee S 2012 High performance optical gating in junction device based on vanadium dioxide thin film grown by sol-gel method *J. Electr. Eng. Technol.* **7** 784–8
- [6] Hoummady M, Campitelli A and Wlodarski W 1997 Acoustic wave sensors: design, sensing mechanisms and applications *Smart Mater. Struct.* **6** 647
- [7] Chu P K and Li L 2015 Characterization of amorphous and nanocrystalline carbon films *J Mater. Chem. Phys.* **96** 253–77
- [8] Akande A A, Liganiso E C, Dhonge B P, Rammutla K E, Machatine A, Prinsloo L, Kunert H and Mwakikunga B W 2015 Phase evolution of vanadium oxides obtained through temperature programmed calcinations of ammonium vanadate in hydrogen atmosphere and their humidity sensing properties *J. Mater. Chem. Phys.* **151** 206–14
- [9] Pagnier T, Boulova M, Galerie A, Gaskov A and Lucazeau G 2000 Reactivity of SnO₂–CuO nanocrystalline materials with H₂S: a coupled electrical and Raman spectroscopy study *Sensors Actuators B* **71** 134–9
- [10] Boulova M, Gaskov A and Lucazeau G 2001 Tungsten oxide reactivity versus CH₄, CO and NO₂ molecules studied by Raman spectroscopy *Sensors Actuators B* **81** 99–106
- [11] Govender M, Motaung D E, Mwakikunga B W, Umapathy S, Sil S, Prasad A K, Machatine A G J and Kunert H W 2013 Operating temperature effect in WO₃ film for gas sensing *2013 IEEE SENSORS* pp 1–4
- [12] Lee S-H, Cheong H M, Seong M J, Liu P, Tracy C E, Mascarenhas A, Pitts J R and Deb S K 2003 Raman spectroscopic studies of amorphous vanadium oxide thin films *Solid State Ion.* **165** 111–6
- [13] Julien C, Nazari A G and Bergstrom O 1997 Raman scattering studies of microcrystalline V₆O₁₃ *Phys. Status Solidi b* **201** 319–25
- [14] Akande A A, Rammutla K E, Dhonge B P, Machatine A G J and Mwakikunga B W 2016 Room temperature methane (CH₄) sensing by vanadium oxide (VO_x) nanoparticles *Adv. Sci. Lett.* **22** 901–4
- [15] Mwakikunga B et al 2013 A classification and ranking system on the H₂ gas sensing capabilities of nanomaterials based on proposed coefficients of sensor performance and sensor efficiency equations *Sensors Actuators B* **184** 170–8
- [16] Simo A, Mwakikunga B, Sone B T, Julies B, Madjoe R and Maaza M 2014 VO₂ nanostructures based chemiresistors for low power consumption hydrogen sensing *Int. J. Hydrog. Energy* **39** 8147–57

- [17] Rao M C 2013 Structural stoichiometry and phase transitions of MoO₃ thin films for solid state microbatteries *Res. J. Recent Sci.* **2** 67–73
- [18] Laubach S, Schmidt P C, Thißen A, Fernandez-Madrigal F J, Wu Q, Jaegermann W, Klemm M and Horn S 2007 Theoretical and experimental determination of the electronic structure of V₂O₅, reduced V₂O_{5-x} and sodium intercalated NaV₂O₅, *Phys. Chem. Chem. Phys.* **9** 2564
- [19] Zhon B and He D 2008 Raman spectrum of vanadium pentoxide from density-functional perturbation theory *J. Raman Spectrosc.* **29** 1475–81
- [20] Adu K W, Gutiérrez H R, Kim U J, Sumanasekera G U and Eklund P C 2005 Confined phonons in Si nanowires *Nano Lett.* **5** 409–14
- [21] Arora A K, Rajalakshmi M, Ravindran T R and Sivasubramanian V 2007 Raman spectroscopy of optical phonon confinement in nanostructured materials *J. Raman Spectrosc.* **38** 604–17
- [22] Fauchet P M and Campbell I H 1988 Raman spectroscopy of low-dimensional semiconductors *Crit. Rev. Solid St. Mater. Sci.* **14** s79–s101
- [23] Mwakikunga B W, Maaza M, Hillie K T, Arendse C J, Malwela T and Sideras-Haddad E 2012 From phonon confinement to phonon splitting in flat single nanostructures: a case of VO₂@V₂O₅ core-shell nano-ribbons *Vib. Spectrosc.* **61** 105–11
- [24] Mwakikunga B W, Sideras-Haddad E, Forbes A and Arendse C J 2008 Raman spectroscopy of WO₃ nano-wires and thermo-chromism study of VO₂ belts produced by ultrasonic spray and laser pyrolysis techniques *Phys. Status Solidi a* **205** 150–4
- [25] Masina B N, Lafane S, Wu L, Akande A A, Mwakikunga B, Abdelli-Messaci S, Kerdja T and Forbes A 2015 Phase-selective vanadium dioxide (VO₂) nanostructured thin films by pulsed laser deposition *J. Appl. Phys.* **118** 165308
- [26] Akande A A 2014 Vanadium dioxide nanostructure and applications in sensors *MSc Thesis* University of Limpopo (Unpublished)
- [27] Sajilal K and Moses Ezhil Raj A 2016 Effect of thickness on physico-chemical properties of p-NiO (bunsenite) thin films prepared by the chemical spray pyrolysis (CSP) technique *Optik* **127** 1442–9
- [28] Huang E *et al* 2002 Pore size distributions in nanoporous methyl silsesquioxane films as determined by small angle x-ray scattering *Appl. Phys. Lett.* **81** 2232–4
- [29] Yu Q, Li W, Liang J, Duan Z, Hu Z, Liu J, Chen H and Chu J 2013 Oxygen pressure manipulations on the metal-insulator transition characteristics of highly (011)-oriented vanadium dioxide films grown by magnetron sputtering *J. Phys D: Appl. Phys.* **46** 055310
- [30] Zang P, Huang T, You Q, Zang J, Li W, Wu J, Hu Z and Chu J 2015 Effects of crystal orientation on electronic band structure and anomalous shift of higher critical point in VO₂ thin films during the phase transition process *J. Phys D: Appl. Phys.* **48** 485302
- [31] Kerber R 2002 Markovnikov's rule in history and pedagogy *Found. Chem.* **4** 61–72
- [32] Xu C, Ma C, Xiao F, Chen H and Dai B 2016 Catalyst-free hydrochlorination protocol for terminal arylalkynes with hydrogen chloride *Chin. Chem. Lett.* **27** 1683–5
- [33] Tepper B, Richer B, Dupuis A C, Kuhlbeck H, Hucho C, Schilbe P, Yarmo A M and Freund H J 2002 Adsorption of molecular and atomic hydrogen on vacuum-cleaved V₂O₅ (001) *Surf. Sci.* **496** 64–72
- [34] Sipr O, Simunek A, Bocharov S, Kirchner Th and Drager G Geometric and electronic structure effects in polarized V K-edge absorption near-edge structure spectra of V₂O₅ *Phys. Rev. B* **60** 14115
- [35] Petrov G I and Yakovlev V V 2002 Raman microscopy analysis of phase transformation mechanisms in vanadium dioxide *Appl. Phys. Lett.* **81** 1023
- [36] Pan M, Liu J, Zhong H, Wang S, Li Z, Chen X and Lu W 2004 Raman study of phase transition in VO₂ thin film *J. Cryst. Growth* **268** 178–83
- [37] Akande A A, Mwakikunga B W, Rammutla K E and Machatine A 2015 Larger selectivity of the V₂O₅ nano-particles sensitivity to NO₂ than NH₃ *Sens. Trans.* **192** 61–5
- [38] Soleimanpour A M, Jayatissa A H and Sumanasekera G 2013 Surface and gas sensing properties of nanocrystalline nickel oxide thin film *Appl. Surf. Sci.* **276** 291–7
- [39] Johnson J L, Behnam A, An Y, Pearton S J and Ural A 2011 Experimental study of graphitic nanoribbon films for ammonia sensing *J. Appl. Phys.* **109** 124301